RESEARCH ARTICLE | JULY 25 2022

Characterizing purely elastic turbulent flow of a semi-dilute entangled polymer solution in a serpentine channel

Pegah Shakeri ; Michael Jung ; Ralf Seemann

Physics of Fluids 34, 073112 (2022)
https://doi.org/10.1063/5.0100419

Physics of Fluids ARTICLE scitation.org/journal/phf

Characterizing purely elastic turbulent flow of a semi-dilute entangled polymer solution in a serpentine channel

Cite as: Phys. Fluids **34**, 073112 (2022); doi: 10.1063/5.0100419
Submitted: 24 May 2022 · Accepted: 4 July 2022 ·
Published Online: 25 July 2022

Pegah Shakeri,[1,2,a)] Michael Jung,[1,2] and Ralf Seemann[1,2]

AFFILIATIONS

[1]Experimental Physics & Center of Biophysics, Saarland University, 66123 Saarbrücken, Germany
[2]Max Planck Institute for Dynamics and Self-Organization, 37077 Göttingen, Germany

[a)]Author to whom correspondence should be addressed: pegah.shakeri@physik.uni-saarland.de

ABSTRACT

Polymer solutions in the semi-dilute regime are of considerable industrial importance. The complex rheological properties of such highly viscoelastic fluids and the complexity of their flow characteristics, especially in curved geometries, necessitate a thorough experimental characterization of the dynamics of such fluid flows. We apply statistical, spectral, and structural analyses to the experimentally obtained velocity fields of a semi-dilute entangled polymer solution in a serpentine channel to fully characterize the corresponding flow. Our results show that at high Weissenberg numbers, yet vanishing Reynolds numbers, the flow resistance is significantly increased, which indicates the emergence of a purely elastic turbulent flow. Spatial flow observations and statistical analysis of temporal flow features show that this purely elastic turbulent flow is non-homogeneous, non-Gaussian, and anisotropic at all scales. Moreover, spectral analysis indicates that compared to elastic turbulence in the dilute regime, the range of present scales of the excited fluctuations is narrower. This is partly due to the entanglement of the polymers in this concentration regime, which restricts their movement, and partly due to the mixed flow type inherent in the serpentine geometry, which can reduce the extent of polymer stretching and, thus, reduce the intensity of the fluctuations in the flow. Furthermore, proper orthogonal decomposition analysis is applied to directly extract the turbulent flow structure and reveals the activity of the counter-rotating vortices associated with secondary flow, which significantly contribute to the total kinetic energy of the flow.

I. INTRODUCTION

Polymer solutions exhibit mechanical properties that are intermediate between viscous liquids and elastic solids due to the elasticity of the polymer molecules and their stretching and relaxation during flow.[1] Such viscoelastic fluids are ubiquitous in a broad range of industrial applications[2–4] and biological settings.[5–8] One of the unique features of viscoelastic fluid flows, particularly in curved flow pathways, is the appearance of an unstable state driven by nonlinear elastic stresses, even in the absence of inertial forces.[9] This phenomenon, known as purely elastic instability or purely elastic turbulence, was first discovered by Giesekus in the Taylor-Couette flow of dilute polymer solutions.[10] The occurrence of purely elastic instability can be beneficial for several industrial applications. For example, the agitation caused by the unstable flow improves mixing capacity and heat transfer.[11,12] Improving the efficiency of capillary entrapment displacement in porous media has also been proven to be related to the occurrence of purely elastic instability during polymer flooding.[13] However, in multiple processes in the food and cosmetics industries[14,15] as well as polymer extrusion,[4] the occurrence of purely elastic instability is rather undesirable. Therefore, the importance of this phenomenon necessitates an understanding of the origin and characterization of purely elastic turbulent flows.

The origin of the purely elastic instability is related to the behavior of polymer molecules.[16–18] In fact, the counter-reaction of the elastic stress loading (deformation) and unloading (relaxation) of the polymers is reflected in the flow, resembling the characteristics of turbulent flow, such as non-parallel streamlines and chaotic fluctuation of flow properties, accompanied by a significant increase in flow resistance.[19] The polymer behavior and, thus, the induced unstable flow features strongly depend on the polymer properties such as molecular weight, size, and concentration, as well as the flow type.[20–23] In the dilute regime below the overlap concentration, the individual

polymer coils are far apart from each other and, hence, do not interact. The behavior of such polymer solutions is governed solely by the dynamics of a single polymer and its interaction with solvent molecules.[1] Although a considerable amount of research has been devoted to the numerical and experimental study of the purely elastic turbulence of dilute polymer solutions,[17,24–35] there are far fewer studies focusing on the semi-dilute entangled polymer solutions,[17,36–38] despite their industrial importance. The polymer behavior above the overlap concentration in the semi-dilute entangled regime is more complicated, as polymers strongly interact with each other and even become significantly entangled. Numerical modeling of such fluid flows in a highly turbulent state is extremely challenging due to the chaotic nature of the expected solution caused by the nonlinear rheological properties and the corresponding flow equations.[39,40] Therefore, understanding and characterizing the purely elastic instability in the semi-dilute concentration regime through experimental research are not only valuable, but essential.

Despite the highly nonlinear and random nature of elastic turbulent flows in general, they are known to be systematic and reproducible on a statistical level.[41–43] A precise and reliable statistical representation of elastic turbulence, however, requires an extensive description of temporal and spatial fluctuations of flow properties. Improvements in particle image velocimetry (PIV), both in hardware and data processing algorithms that allow high temporal and spatial resolution data acquisition, make this technique one of the most attractive and successful tools in turbulent fluid flow dynamics.[44–46] The acquired time-resolved velocity fields provide in-depth information on the turbulent flow, which can be further processed using various statistical and numerical methods to extract the stochastic turbulent features and structure. A number of studies restricted to dilute polymer solutions have already used the PIV technique to characterize the corresponding purely elastic turbulence in various geometries with curved pathways.[18,32,47,48]

Most statistical analyses of elastic turbulence are based on the flow fluctuations at fixed points either in time or in space and rely on the Taylor frozen turbulence hypothesis to relate the temporal and spatial characteristics of elastic turbulence.[18,49,50] The Taylor hypothesis suggests that in homogeneous flows, turbulent fluctuations travel downstream without changing their properties.[51] However, the global validity of this hypothesis has been experimentally and numerically questioned in the elastic turbulence of dilute polymer solutions.[27,50] To avoid the Taylor hypothesis and directly extract the spatial features and structure of turbulent flow, the proper orthogonal decomposition (POD) method was developed in the field of fluid dynamics.[52] POD is a robust order reduction method for decomposing the fluctuations in a flow field into a set of energy modes to represent them as a set of basis functions. As a result, the highly complex problem can be reduced to a simpler one by considering only the modes with the highest energy that contributes the most to the turbulent flow. The application and practical utility of POD analysis to direct numerical simulation (DNS) results of elastic turbulence of dilute polymer solutions have been demonstrated in the literature for both high[53,54] and vanishing Reynolds numbers, Re (ratio of inertial to viscous forces).[55] However, the application of POD in the analysis of experimentally acquired dynamics of an elastic turbulent flow has not yet been reported.

In this work, we investigate the flow of a semi-dilute entangled polymer solution in a microfluidic serpentine geometry using the μPIV technique with the aim of providing a comprehensive characterization of the purely elastic turbulent flow observed at relatively high Weissenberg numbers (ratio of elastic to viscous forces) yet at vanishing Reynolds numbers. In our experiments, three different stages of the flow are considered, namely, below, near, and safely above the onset of purely elastic instability, to study the evolution of the purely elastic turbulent flow. Furthermore, to evaluate the homogeneity and stream-wise dependence of the flow features at the highly turbulent stage, we compare the velocity profile and spatial flow features at five different positions in the serpentine channel. Common statistical analyses, including single-point statistics and two-point correlation, are employed to characterize purely elastic turbulent flow features of semi-dilute entangled polymer solutions in the serpentine channel. Furthermore, we directly extract the structure of purely elastic turbulent flow in the serpentine channel, for the first time to the best of our knowledge, by applying the POD method to the instantaneous velocity fields captured experimentally using μPIV.

The structure of this paper is as follows: We explain the proper orthogonal decomposition method in Sec. II and sample preparation methods, rheological properties of the fluid, and the experimental setup and procedure in Sec. III. The experimental results are presented and discussed in Sec. IV and concluded in Sec. V.

II. PROPER ORTHOGONAL DECOMPOSITION

Proper Orthogonal Decomposition (POD) also known as principal component analysis is a numerical order reduction technique that decomposes a set of instantaneous velocity fields into a set of deterministic basis functions or modes.[52,56,57] In the following, we briefly present the basic concept of this method, which is necessary to comprehend this work. Further mathematical details and application of this method in fluid dynamics of the turbulent flow can be found in the literature.[52,56,58–60] In the case of an experimentally acquired flow field with high spatial resolution, the POD method is applied using the "snapshot method."[61] As its name suggests, this method treats each velocity field obtained from μPIV as a snapshot. In each snapshot, the velocity vector is defined as $\mathbf{u} = (u, v)$ and each velocity component (scalar) is both a function of position (x, y) and time. The proper orthogonal decomposition can be applied to either component as well as to the magnitude of the velocity $|\mathbf{u}| = \sqrt{u^2 + v^2}$. The numerical analysis begins with constructing a $m \times n$ matrix, $\mathbf{U}$, from the velocity components, e.g., $u(x, y, t)$, where $m = N_t$ and $n = N_x \times N_y$, with N_t being the number of snapshots and N_x, N_y being the number of spatial vectors in x- and y-directions. In fact, each entry (u_{ij}) of the matrix $\mathbf{U}$ is the measured velocity at a point j in space at time i,

$$\mathbf{U} = \begin{bmatrix} u_{11} = u(x_1, y_1, t_1) & \cdots & u_{1n} = u(x_{N_x}, y_{N_y}, t_1) \\ u_{21} = u(x_1, y_1, t_2) & \cdots & u_{2n} = u(x_{N_x}, y_{N_y}, t_2) \\ \vdots & \vdots & \vdots \\ u_{m1} = u(x_1, y_1, t_m) & \cdots & u_{mn} = u(x_{N_x}, y_{N_y}, t_m) \end{bmatrix}.$$

A POD decomposition of the matrix $\mathbf{U}$ aims to find a set of orthogonal vectors $[\mathbf{\Phi}^{(1)}(x, y), \mathbf{\Phi}^{(2)}(x, y), \ldots, \mathbf{\Phi}^{(N_t)}(x, y)]$ such that

$$\mathbf{U}(x, y, t) = \mathbf{U}_1(x, y, t) + \sum_{n=2}^{N_t} \mathbf{a}^{(n)}(t) \cdot \mathbf{\Phi}^{(n)}(x, y), \tag{1}$$

where $\mathbf{U_1}(x, y, t)$ represents the time averaged velocity over all N_t snapshots. $\mathbf{\Phi}^{(n)}$ are the eigenvectors of the auto-covariance matrix

$\mathbf{C} = 1/(m-1)\mathbf{U}^T\mathbf{U}$, and $\mathbf{a}^{(n)}$ are their corresponding temporal coefficients. These eigenvectors, known as *proper orthogonal modes* of the velocity fluctuations, can be viewed as the axes of an n-dimensional ellipsoid enclosing the entire data set (matrix $\mathbf{U}$) in an n-dimensional space.[62] Moreover, since the coefficients $\mathbf{a}^{(n)}$ are uncorrelated, each one can be interpreted as variations of one independent "mode" of fluctuation. The energy contribution of each mode, $[i = 1, \ldots, N_t]$ to the total kinetic energy (TKE), is calculated as $E_i = \lambda_i / \sum_{k=1}^{N_t} \lambda_k$, where λ_i are the corresponding eigenvalues in the descending order.

III. EXPERIMENTAL METHODS

A. Working fluid and its rheological properties

In this study, we used a viscoelastic aqueous solution containing 2000 ppm (0.2 *w*%) of partially hydrolyzed polyacrylamide (HPAM) Flopaam 3630 (SNF Floerger) with a molecular weight of (18.7 ± 2.0) MDa. The polymer solution was diluted following a standard protocol[13,63] from a 5000 ppm stock solution in a "brine" solution composed of ultrapure water with 1000 ppm NaCl and 100 ppm $CaCl_2$. Since HPAM polymers are widely used for enhanced oil recovery, where salt is an essential component of the injected polymer solutions, we have included the typical salt type and concentration considered in the literature.[37,38,64] As shown in our previous study,[65] the selected salt concentration is in the low salt range and does not have a significant impact on screening the negative charges of the polymers' backbone or causing transient cross-linking network. Using a pycnometer, the density of the polymer solution was determined as $\rho_P = (1.00 \pm 0.01)$ g/cm^3. Because the polymer concentration used in our microfluidic experiments was about 25 times larger than the polymer's overlap concentration of $c^*_{3630} \approx 82$ ppm, we can safely assume it to be in the semi-dilute entangled regime.[65] The shear rate, $\dot{\gamma}$, dependent viscosity, $\eta(\dot{\gamma})$, and the first normal stress difference, $N_1(\dot{\gamma})$, of the polymer solution at (20±0.2)°C were measured by a steady shear step test applying a standard protocol in the deformation rate-controlled mode using a HAAKE MARS 40 rheometer and a 60 mm cone plate geometry with an angle of 1°. The rheological data are plotted in Fig. 1(a). The storage modulus, G', and loss modulus, G'', determined from small amplitude frequency sweep tests in the stress-controlled mode are plotted in Fig. 1(b). The crossover happens at the frequency of $\omega \approx (0.35 \pm 0.1)$ Hz; thus, the longest relaxation time of the polymer solution is determined as $\lambda_{\max} = 1/\omega \approx (3 \pm 1)$ s. The experimental data are fitted to the multi-mode Maxwell model.[65]

B. Viscoelastic fluid model

To define the relevant dimensionless Weissenberg number and to evaluate viscoelastic flow, we need to choose a constitutive fluid model, which best represents the rheological properties of the fluid. Among all models developed for describing semi-dilute polymer solutions,[66] the White-Metzner (WM) constitutive model could best represent the strong shear-thinning and non-quadratic first normal stress difference of our polymer solution (Fig. 1). It should be noted that the WM consecutive model assumes that the second normal stress difference, N_2, is zero and does not consider extensional viscosity. In polymer melts and highly entangled polymer solutions, N_2 can be significant and is typically exerted in the opposite direction of N_1; thus, it can dampen elastic instability and suppress secondary flows in curved ducts. However, since for polymer solutions in the semi-dilute regime, as used in this work, the magnitude of N_2 is typically measured to be in the range of 1% to a maximum of 10% of N_1, we assume that N_2 can be neglected.[67] Moreover, the flow in a serpentine channel is mainly shear dominated; thus, the effect of extensional viscosity can also be safely excluded. Therefore, the choice of the WM fluid model in our case is reasonable. The basic concept of the WM model is to define a total stress tensor $\boldsymbol{\tau} = \boldsymbol{\tau}_1 + \boldsymbol{\tau}_2$ and a total viscosity $\eta = \eta_1 + \eta_2$ that are related to the deformation rate tensor $\mathbf{D} = \frac{1}{2}(\nabla\mathbf{u} + \nabla\mathbf{u}^T)$.[9,40,68] The pure viscous component of the stress tensor $\boldsymbol{\tau}_2$ is defined as $\boldsymbol{\tau}_2 = 2\,\eta_2\,\mathbf{D}$, where η_2 is the solvent viscosity. $\boldsymbol{\tau}_1$ is defined by

$$\boldsymbol{\tau}_1 + \lambda(\dot{\gamma})\overset{\nabla}{\boldsymbol{\tau}}_1 = 2\,\eta_1(\dot{\gamma})\,\mathbf{D}, \tag{2}$$

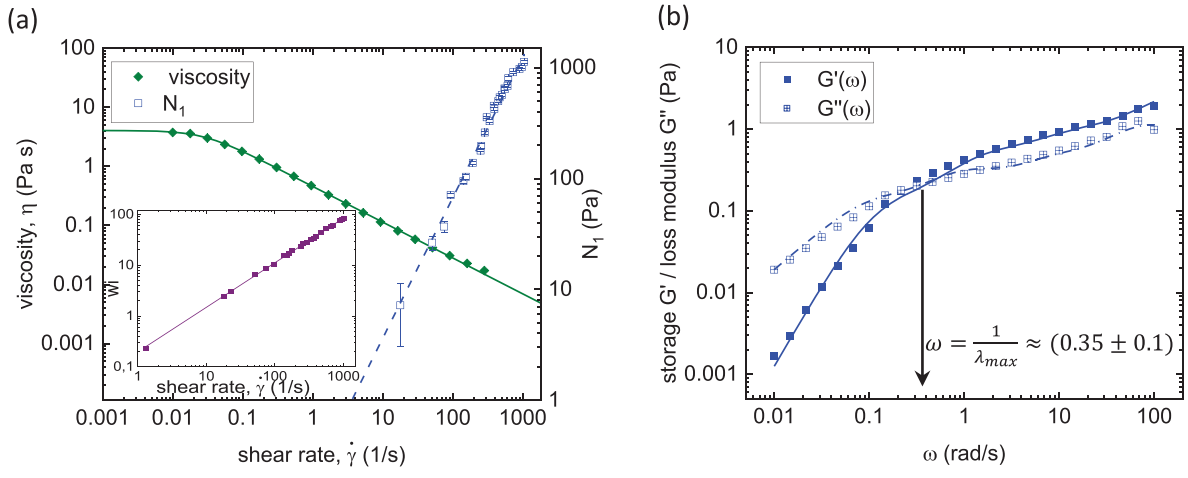

FIG. 1. (a) The (shear) viscosity $\eta(\dot{\gamma})$ (green diamonds) and first normal stress difference N_1 (□) measured using a rotational rheometer. The solid and the dashed lines are (olive green) fit to the Carreau-Yasuda model Eq. (4) and a power law (blue) $N_1(\dot{\gamma}) = (0.34 \pm 0.07)\dot{\gamma}^{(1,19\pm0,03)}$, respectively. The inset shows the calculated *Wi* (purple squares) based on Eq. (5). The solid line (purple) is a power law fit, $Wi(\dot{\gamma}) = (0.15 \pm 0.01)\dot{\gamma}^{(0.91\pm0.01)}$. (b) Elastic modulus G′ (blue squares) and loss modulus G″ (⊞) measured via small amplitude frequency sweep test. Solid and dashed lines are corresponding fits to the multi-mode Maxwell model with four elements.

where $\overset{\nabla}{\boldsymbol{\tau}}_1$ is the upper convected time derivative and $\lambda(\dot{\gamma})$ is the shear dependent relaxation time calculated as

$$\lambda(\dot{\gamma}) = N_1/2(\eta(\dot{\gamma}) - \eta_\infty)\dot{\gamma}^2, \tag{3}$$

where the shear rate is defined as $\dot{\gamma} = \sqrt{2\,tr(\mathbf{D}^2)}$. The shear dependent total viscosity of the polymer solution $\eta(\dot{\gamma})$ is described by the Carreau–Yasuda model,[9,69]

$$\eta(\dot{\gamma}) - \eta_\infty = (\eta_0 - \eta_\infty)\left[1 + (\Lambda\dot{\gamma})^a\right]^{\frac{n-1}{a}}, \tag{4}$$

where η_0 and η_∞ are the zero-shear viscosity and the viscosity at infinite shear rates, Λ is a characteristic time, n is the power law exponent associated with the degree of shear thinning, and a is a transition control factor. The Weissenberg number, Wi, which is defined as $Wi(\dot{\gamma}) = \lambda(\dot{\gamma})\dot{\gamma}$, is thus calculated as

$$Wi(\dot{\gamma}) = N_1/2(\eta(\dot{\gamma}) - \eta_\infty)\dot{\gamma}. \tag{5}$$

Since, in our study, the Reynolds number is always safely below one, inertia forces are negligible, and the observed flow features are merely related to elastic stresses. Therefore, the Weissenberg number Wi is the relevant dimensionless number to be considered in this case. The calculated values of Wi as a function of the shear rate are plotted in the inset of Fig. 1.

C. Microfluidic geometry

The flow geometry used in all experiments was a microfluidic serpentine channel consisting of 33 consecutive half-bends with a total length of $l \approx 26$ mm, a width of $w \approx 0.125$ mm, a height of $h \approx 0.04$ mm, and an inner bend radius of $r_i \approx 0.125$ mm, see the sketch in Fig. 2. The microscale geometry allows us to achieve high Wi while keeping the Re low. It is worth mentioning that the choice of the serpentine channel as flow geometry is twofold. On the one hand, curved channels are significant for industrial and biological viscoelastic fluid flows. On the other hand, despite its simplicity, the flow type in the serpentine channel is complex and leads to intriguing phenomena in polymer dynamics and the structure of the flow.

The positive master of the microfluidic device was fabricated via standard photo lithographic protocols.[70] A negative mold was fabricated from that using Sylgard 184 (Dow Corning). In a second molding step, the final microfluidic device was made using the stiff, oil resistant, photo-reactive resin NOA 83H (Norland optical adhesives) sealed with a microscopy glass slide and sandwiched with an additional coverslip to enhance the stability and avoid deformation of the channel at higher pressures.

D. Experimental protocol and μPIV setup

The microfluidic channel described in Sec. III C was used as the flow geometry in this work. The inlet of the microfluidic device was connected to a microfluidic pressure pump (MFCS-EZ, Fluigent) that enabled fluid injection at a controlled pressure. The outlet was connected to a liquid reservoir at the same height as the microfluidic device to avoid gravitational counterpressure. The microfluidic device was placed on an epifluorescent inverted microscope (Axio observer Z1, Zeiss) equipped with a 20× air objective (Plan-Apochromat, Zeiss) with numerical aperture NA = 0.8. Fluorescent polystyrene microspheres ($\lambda_{ext} = 542$ nm $/\lambda_{emt} = 612$ nm; FlouroMax, Thermo Fisher) with a diameter of 1 μm were added to the polymer solution. The size of these particles was large enough to achieve an acceptable signal-to-noise ratio but small enough to ensure that they followed the flow with minimal delay without affecting it. The flow in the serpentine channel was illuminated with a triggered Continuous Wave (CW) laser ($\lambda = 532$ nm, LaVision), and the light from the fluorescent particles was captured via a sCMOS camera (Imager pro HS, PCO) with a resolution of ≈ 3 pixel/μm after passing through a cutoff filter to isolate the emission signal and reduce the background noise. A sketch of the μPIV setup is shown in Fig. 2(a).

To ensure that the recorded images correspond to the steady state flow and not to the transient regime, the recording was started at least 20 min after applying the pressure at the inlet. Double-frame images were captured with small-time delay dt in the range of 0.1–0.8 ms, depending on the flow velocity, to achieve a particle shift of no more than five pixels between consecutive double-frames. The imaging

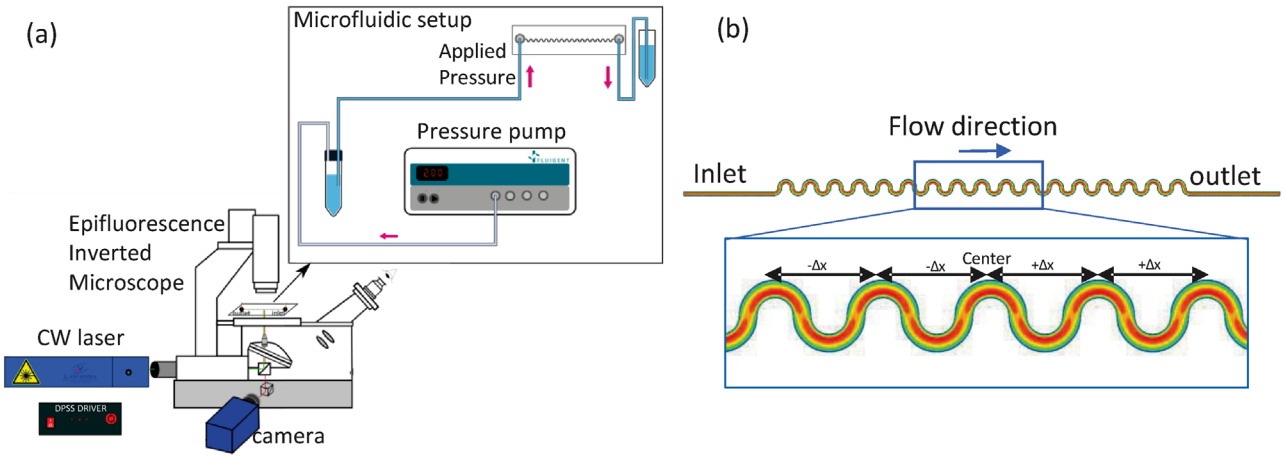

FIG. 2. (a) Sketch of the experimental setup including μPIV. (b) Sketch of the microfluidic geometry with dimensions of $w \approx 0.125$ mm, height of $h \approx 0.04$ mm, and an inner bend radius of $r_i \approx 0.125$ mm. The center corresponds to a point 13 mm downstream of the inlet and $\Delta x = 1$ *mm*.

frequency, based on each pair of double-frames, was set to 42 Hz for all experiments, and a sequence of 2100 double-frames, equivalent to a duration of 50 s, ≈17 times longer than the polymer's longest relaxation time, was recorded at multiple locations in the channel, i.e., at different locations along the channel by focusing on the mid-height plane of the channel [Fig. 2(b)]. The depth of correlation,[71] δz, based on the optical properties of the objective, laser wavelength, and particle size used in our experiments, is computed as $\delta z \approx 5\,\mu$m for our setup. This corresponds to roughly 12% of the channel height. All experiments were conducted at a room temperature of $(20 \pm 1)^{\circ}$C.

To compute the velocity fields from the μPIV images using a cross-correlation algorithm, the individual images of the double-frames were first divided into square areas called "interrogation windows." A multi-pass processing approach with an initial interrogation window size of (64 × 64) pixel, and 50% overlap to a final interrogation window size of (24 × 24) pixel with 75% overlap was considered to improve the accuracy of the fast Fourier transform (FFT) cross-correlation algorithm.[72] The experimental setup and the processing routine were tested with a 50 w% aqueous glycerin solution. The difference between the μPIV results of the test experiments and the corresponding computational fluid dynamic (CFD) simulation was less than 5%.

IV. RESULTS AND DISCUSSION

In the following, we present and discuss the experimental results. First, we study the transition from laminar to elastic turbulent flow and identify the onset of purely elastic instability. Then, we investigate the spatial dependence of the velocity profile on the position in the laminar and turbulent stages of the flow. Thereafter, the purely elastic turbulent flow is characterized at different probing positions using single-point statistics in the time domain and two-point correlation analyses. Finally, we extract the flow structure at the highest turbulent stage of our system using the POD method.

A. Evolution of the purely elastic turbulent flow and flow features

1. Onset of purely elastic instability

To study the flow evolution from the laminar to turbulent state, the pressure applied at the inlet was stepwise increased, and instantaneous velocity fields were captured at the center of the serpentine channel, approximately 13 mm downstream of the channel inlet [Fig. 2(b)]. In all experiments, the microscope focus was set at the mid-height of the channel. Examples of the time-averaged velocity fields and their corresponding root-mean-square distribution at two stages of the flow, corresponding to the lowest and the highest applied inlet pressures, are shown in Fig. 3. At lower applied inlet pressure, the velocity field is laterally symmetric [Fig. 3(a)] with negligible rms values [Fig. 3(b)], indicating a laminar flow. However, the velocity field corresponding to the highest applied inlet pressure is clearly asymmetric [Fig. 3(c)], with a significant rms distribution [Fig. 3(d)].

The time averaged velocity as a function of the applied inlet pressure, respectively, Weissenberg number, at a normalized vertical position of $\varepsilon = 0$ at the center of the channel is plotted in Fig. 4(a). The shear rate in the serpentine channel is approximated by $\dot{\gamma} = 4\langle|\mathbf{u}|\rangle/r$,[65,73]

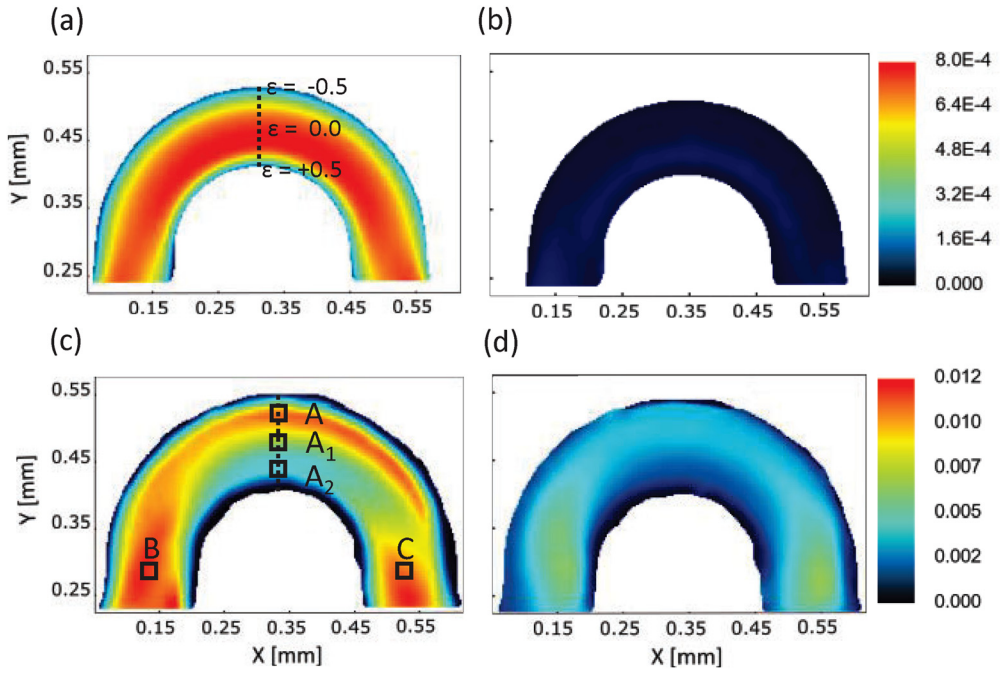

FIG. 3. (a) Time averaged velocity field at the mid-height of the channel at the central half-bend for an inlet pressure of 3.47 kPa ($Wi \approx 5 < Wi_{crit}$), $\varepsilon = (0.5w - y)/w$ is the normalized vertical position across the channel width; (b) the corresponding time averaged root mean square values of the velocity field; (c) time averaged velocity fields at the center of the serpentine channel for an inlet pressure of 56.39 kPa ($Wi \approx 45 > Wi_{crit}$). Points ($A$), ($A_1$), and ($A_2$) along the central vertical line at $\varepsilon = -0.3$, $\varepsilon = 0.0$, and $\varepsilon = +0.3$, respectively, and points (B) and (C) at the lateral ends of the half-bend are probing positions. Point (A) represents the region with the highest average velocity, and points (B) and (C) represent the regions with the highest rms value; and (d) the corresponding time averaged root mean square values of the velocity field.

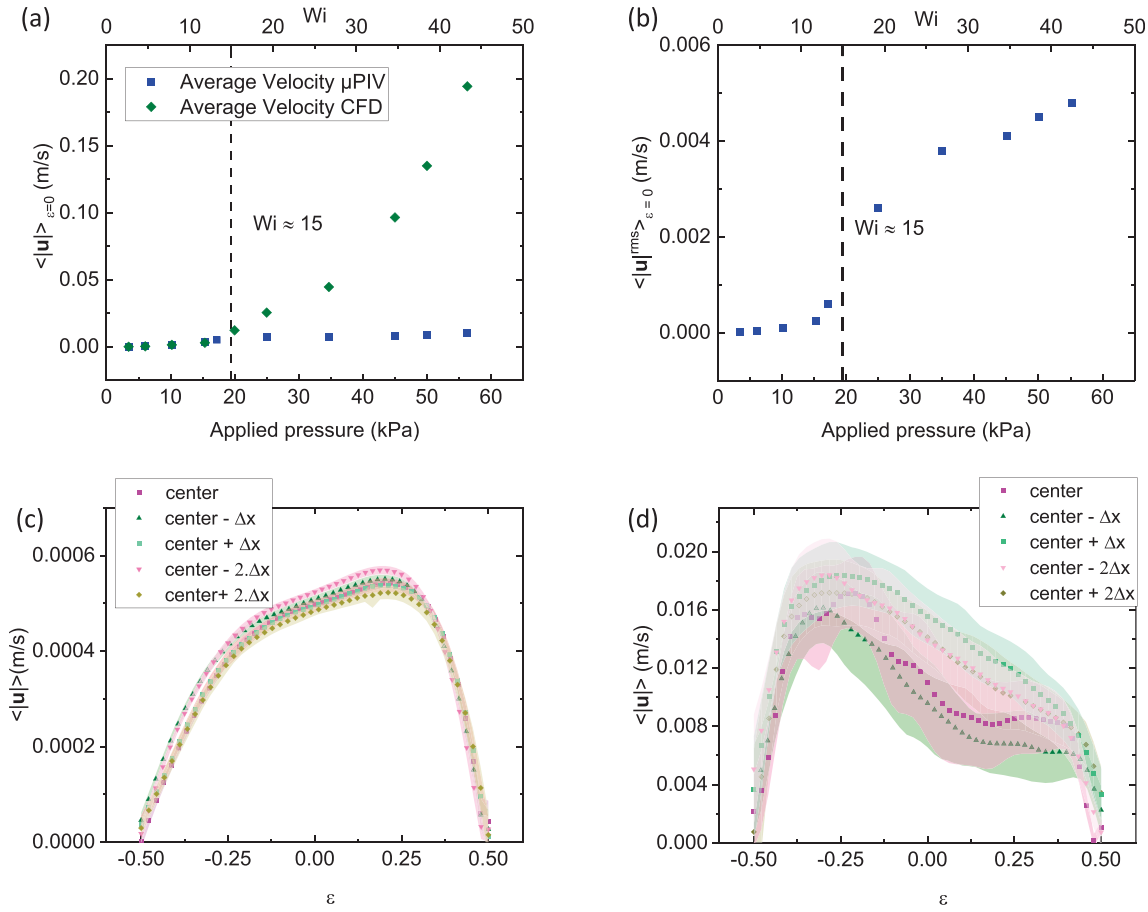

FIG. 4. (a) Time averaged velocity and (b) the corresponding root-mean-square values at $\varepsilon = 0$ at the center of the serpentine channel as the function of applied inlet pressure (bottom axis) and corresponding Weissenberg number (*Wi*, top axis). (c) Time averaged velocity profiles for an inlet pressure of 3.47 kPa ($Wi \approx 5 < Wi_{crit}$), and (d) for the inlet pressure of 56.39 kPa ($Wi \approx 45 > Wi_{crit}$) at five different positions with respect to the center (($\Delta x = 1\ mm$) of the serpentine channel.

with $\langle|\mathbf{u}|\rangle$ and $r = \sqrt{(w\,h)/\pi}$ being the time-averaged velocity and the equivalent radius, respectively. The corresponding Weissenberg number is then calculated based on Eq. (5) for the approximated *in situ* shear rates.

Above a critical inlet pressure, corresponding to $Wi_{crit} \approx 15$, as shown in Fig. 4(a), the measured time averaged velocities determined at the center of the channel fall significantly below numerical values. The numerical values are predicted based on CFD simulations of an imaginary shear thinning fluid with similar Carreau–Yasuda fitting parameters but no elasticity component, using a generalized Newtonian fluid model. Moreover, the experimental root-mean-square (rms) values of the corresponding time-averaged velocities, shown in Fig. 4(b), exhibit a dramatic increase above $Wi_{crit} \approx 15$ as well. These observations indicate an increased flow resistance and large velocity fluctuations, which are characteristics of an unstable flow. To ensure that inertia is negligible throughout the geometry and does not contribute to this unstable flow, we estimate the relevant Reynolds numbers. The used serpentine geometry with the rectangular cross section requires the consideration of two Reynolds numbers. For channel flows, the Reynolds number is usually defined as $Re_c = \varrho\,\langle|\mathbf{u}|\rangle\,r/\eta$, where the equivalent radius, r, is employed as the characteristic length. To account for centrifugal inertia in the curvilinear flow, the radius of the curvature of the serpentine channel, r_i, is used as the characteristic length, and the corresponding Re number can be, thus, expressed as $Re_s = \varrho\,\langle|\mathbf{u}|\rangle\,r_i/\eta$. The maximum Reynolds numbers in our experiments are $Re_c \approx 0.05$ and $Re_s \approx 0.16$, respectively, and we can conclude that the contribution of inertia to the flow is negligible, and the observed unstable flow is a purely elastic turbulent flow related solely to the anisotropic elastic stresses associated with the highly viscoelastic polymer solution.

2. Spatial features of purely elastic turbulent flow

After analyzing the global flow behavior for shear rates below and above the critical shear rate, we additionally aim at the analyzing dependence of the flow profile on the location in the channel, and the spatial homogeneity of the flow. To this end, we repeated the μPIV recordings at four additional positions [Fig. 2(b)], with $\pm\Delta x, \pm 2\,\Delta$ being the distance from the center, ($\Delta x = 1\ mm$, based on the periodicity of our serpentine channel) at two different stages, i.e., at $Wi < Wi_{crit}$ and $Wi > Wi_{crit}$. The velocity profiles across the channel

width along a vertical centerline in each half-bend are plotted in Figs. 4(c) and 4(d), for $Wi \approx 5 < Wi_{crit}$ and for $Wi \approx 45 > Wi_{crit}$, respectively. At $Wi < Wi_{crit}$, the polymer flow in the serpentine channel is laminar, i.e., the flow lines follow the curvature of the channel. The velocity profile at this stage is similar to that of a Newtonian fluid, which means it is skewed toward the wall with the highest curvature, i.e., at $\varepsilon = (0.5w - y)/w > 0$, where the shear rate is higher. Furthermore, velocity profiles at different locations have an identical shape, with negligible difference within the experimental error. In contrast, the velocity profiles corresponding to $Wi > Wi_{crit}$ [Fig. 4(d)] show reversed skewness and are rather shifted to the opposite wall, i.e., $\varepsilon < 0$. This deviation from a laminar flow behavior clearly points toward the presence of flow structures other than the primary streamwise flow. The structure of the flow will be discussed in Sec. IV C. The shape of the velocity profiles is rather irregular and exhibits spatial dependence, which means that the mean flow is not essentially invariant and, thus, the flow is spatially non-homogeneous.

3. Flow topology and its impact on polymer behavior and flow features

The explanation for the observed unstable, non-homogeneous flow of a semi-dilute entangled polymer solution is multifaceted due to the interdependence of fluid and flow properties. Therefore, we first require a lucid insight into the origin of the observed unstable flow, determined by the molecular behavior of the polymers, with respect to the flow geometry. As discussed in the literature,[16–18,74] the purely elastic instability in polymer solutions is driven by the dynamics of the polymers' deformation, which, in turn, is highly dependent on the flow type. In fact, Shaqfeh argues that the ratio between the vorticity and rate of deformation, i.e., the flow type in the flow geometry is a decisive factor for polymer behavior.[22] A practical dimensionless number to define the flow type is the topology factor defined as $\xi = (|\boldsymbol{D}| - |\boldsymbol{\Omega}|)/(|\boldsymbol{D}| + |\boldsymbol{\Omega}|)$, where $|\boldsymbol{D}|$ is the magnitude of the deformation rate tensor and $|\boldsymbol{\Omega}|$ is the magnitude of the vorticity tensor. Polymers exposed to different flow types deform intrinsically different. When subjected to low to moderate shear, the polymers remain in their coiled configuration and align with the flow direction at high shear rates. Extensional flow stretches the polymers, while rotational flow tends to restore them to their coiled shape.[22] The topology factor distribution calculated from experimental values at $Wi \approx 5 < Wi_{crit}$ and $Wi \approx 45 > Wi_{crit}$ is shown in Fig. 5. Below the onset of purely elastic instability, three distinguished regions of shear (green), extensional (red), and rotational (blue) are visible, alternating orderly between successive half-bends. The corresponding histogram of the topology factor distribution indicates that the flow is mainly shear dominated with defined extensional regions. This suggests that polymers remain mainly in their coiled configuration, and thus, the flow is predominantly laminar. For $Wi > Wi_{crit}$, these well-defined regions are no longer distinguishable, and the flow types are rather randomly distributed. The corresponding probability distribution indicates that the fraction of rotational (vortical) flow has increased. This random distribution of flow types combined with their impact on polymer behavior results in spatial non-homogeneity of the flow. Furthermore, the significant contribution of randomly distributed rotational flow type suggests that the purely elastic turbulent flow is anisotropic. However, as Haward *et al.* noted, the topology factor can be dubious

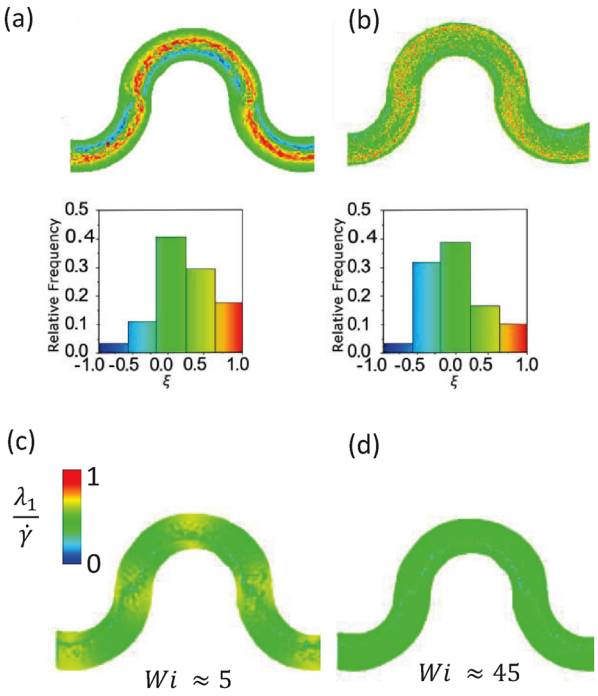

FIG. 5. Local distribution of the topology factor ξ along the serpentine channel ξ (top) and their corresponding probability distribution (bottom) at $Wi \approx 5 < Wi_{crit}$ (a) and at $Wi \approx 45 > Wi_{crit}$ (b). The value $\xi = -1.0$ (blue) indicates a pure rotational flow, $\xi = 0.0$ (green) a pure shear flow, and $\xi = 1.0$ (red) a pure extensional flow. The normalized principal strain rate $(\lambda_1/\dot{\gamma})$ at $Wi \approx 5 < Wi_{crit}$ (c) and $Wi \approx 45 > Wi_{crit}$ (d). The red color in the legend $(\lambda_1/\dot{\gamma} = 1)$ indicates strong extension.

because it does not necessarily contain information about the strength of the flow types, which is very important for the polymer behavior.[75] To this aim, the extensional flow strength is quantified in terms of the principal strain rate parameter λ_1, which is the eigenvector of the deformation rate tensor and is expressed as $\lambda_1 = \frac{1}{2}\sqrt{(D_{11} - D_{22})^2 + 4D_{12}^2}$. The normalized value of $\lambda_1/\dot{\gamma}$ is plotted in Figs. 5(c) and 5(d). As can be seen, even though distinct extensional regions are visible in the topology-factor distribution [Fig. 5(a)], the strength of the extension is quite weak [Fig. 5(c)] and even weaker at the higher Weissenberg number [Fig. 5(d)]. Thus, the flow remains shear dominated across the range of the considered Weissenberg number.

In the semi-dilute entangled regime, the complexity of the rheological properties of the fluid plays an important role in the flow properties as well. Shear thinning, for example, causes a non-parabolic velocity profile and, thus, strong transversal variation of the shear rate in the channel. This leads to different velocities and relaxation times and to different degrees of deformation and relaxation of the polymer at different points in the channel. Moreover, the deformation exerted on the polymers at a given shear rate is stored in them, due to their significant memory effect, before they relax or deform at a different shear rate. This further affects the spatial distribution of rheological properties.

As a result, the mixed and random distribution of the flow types in a serpentine channel in combination with the highly complex rheological behavior of semi-dilute entangled polymer solutions leads to a non-homogeneous and anisotropic purely elastic turbulent flow.

B. Temporal features of purely elastic turbulent flow

To characterize the temporal features of the observed purely elastic turbulent flow, we conduct point-wise analysis of the velocity fluctuations. The velocity fluctuations, $u'(x,y,t)$, are the Reynolds decomposition of the velocity in the form of $u'(x,y,t) = u(x,y,t) - \langle u(x,y)\rangle$, where $u(x,y,t)$ is the instantaneous velocity and $\langle u(x,y)\rangle$ is the time averaged velocity at any point in the 2D domain. We extract time series of velocity fluctuations at three locations along the centerline of the channel, shown as the dashed line in Fig. 3(c), namely, (A) near the outer wall with the largest radius of curvature ($\varepsilon = -0.30$), (A_1) in the middle of the channel ($\varepsilon = 0.0$), and (A_2) near the inner wall with the smallest radius of the curvature ($\varepsilon = +0.30$). It should be noted that these points are chosen at the vertical centerline for convenience, since here the x and y directions correspond to the azimuthal (streamwise) and radial (transversal) directions, respectively.

1. Single-point statistics

The corresponding vertical and horizontal components of the velocity fluctuations, u'_x and u'_y, as a function of time, are shown in Figs. 6(a) and 6(b). The fluctuations in the streamwise direction, u'_x, are significantly stronger than the fluctuations in the transversal direction, u'_y. This observation, which indicates that the temporal velocity fluctuations are anisotropic, is further evident in the statistical moments of the velocity fluctuations at these points, shown in Table I. The values of skewness, S_x and S_y, and kurtosis, K_x and K_y, at different locations suggest that the velocity fluctuations are slightly non-Gaussian. It is worth noting that the higher value of the kurtosis of the streamwise velocity fluctuations near the walls indicates that the fluctuations at these regions are intermittent, i.e., the velocity fluctuations contain a random sequence of violent bursts also known as rare events.[32] The normalized (auto)-correlation function of total velocity fluctuations at points (A), (A_1) and (A_2) computed as $r_{ij}(\tau) = \langle u'_i(t+\tau)u'_j(t)\rangle / \langle u'_i \cdot u'_j(t)\rangle$, and $i = j$, is plotted in Fig. 6(c). The corresponding characteristic time $T = \int_0^\infty r_{ii}(\tau)d\tau$ is on the order of the polymer's longest relaxation time and depends on the position of the probing point. This variation in characteristic time can be explained in view of the shear dependency of the polymer relaxation time in the semi-dilute entangled regime. Near the walls, where the shear rate is highest, the characteristic timescale is smaller than at the center where the shear rate is lower.

2. Two-point correlation

The total temporal velocity fluctuations at points (A), (B), and (C) are extracted, and two-point correlation and spectral analysis are applied to obtain further statistical information about the flow. Point (A) represents the region with the highest average velocity, and points (B) and (C) represent the regions with the highest rms value [Fig. 3(c)]. The normalized velocity fluctuations at these points are shown in Figs. 7(a)–7(c). The presence of random "bursts," an

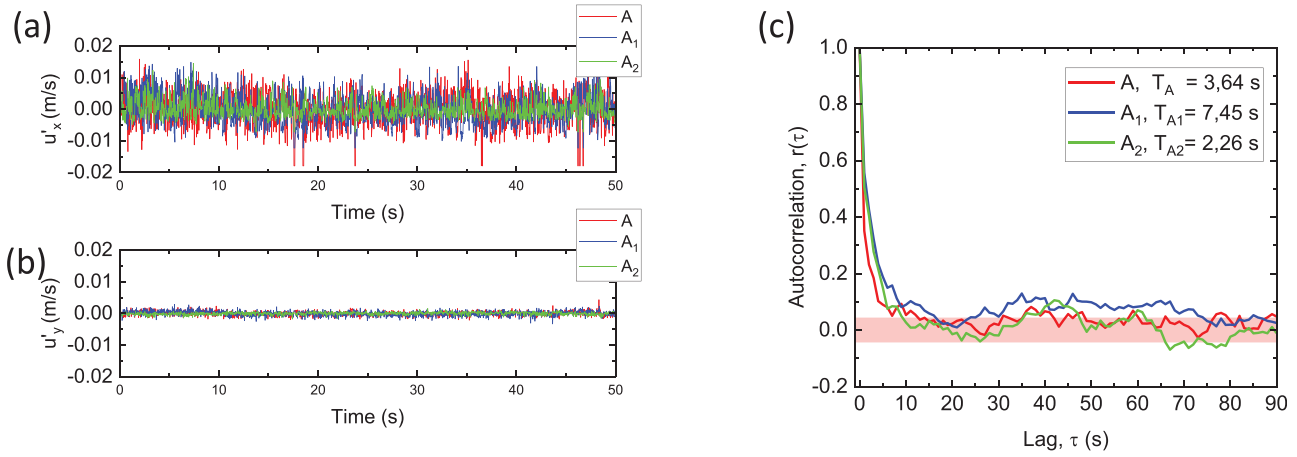

FIG. 6. Temporal fluctuations of (a) streamwise velocity component, (b) transversal velocity component, and (c) autocorrelation function of total velocity fluctuations at points (A), (A_1), and (A_2) marked in Fig. 3(b). The colored rectangle indicates the confident band.

TABLE I. First to fourth moments of velocity fluctuations at $Wi \approx 45$ above the onset of purely elastic instability at three different points (A), (A_1), and (A_2) located along the central vertical line [Fig. 3(c)]. $\langle u'_x\rangle$, $\langle u'_y\rangle$ first moment (mean), σ_x, σ_y second moment (standard deviation), S_x,S_y third moment (skewness), and K_x, K_y fourth moment (kurtosis) of, respectively, x and y components of velocity fluctuations.

Sampling location	$\langle u'_x\rangle$ (m/s)	σ_x (m/s)	S_x	K_x	$\langle u'_y\rangle$ (m/s)	σ_y (m/s)	S_y	K_y
A	3.2040×10^{-6}	0.0052	−0.4822	0.8367	3.3270×10^{-10}	7.4540×10^{-4}	−0.07308	0.43032
A_1	-4.780×10^{-8}	0.0049	0.2763	−0.2681	-1.534×10^{-10}	6.712×10^{-4}	0.1995	0.8450
A_2	-9.2708×10^{-7}	0.0027	0.8538	1.2531	7.3841×10^{-11}	4.1440×10^{-4}	−0.3780	0.4673

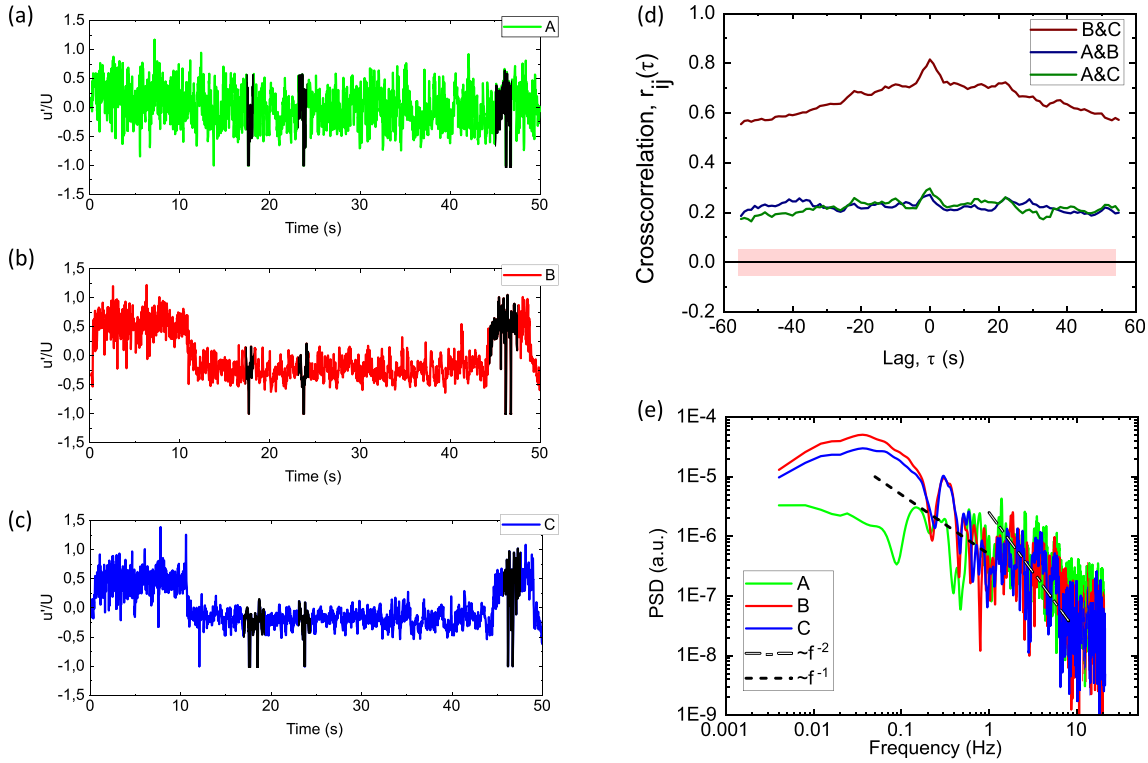

FIG. 7. Normalized total velocity fluctuations at (a) point (*A*), (b) point (*B*), and (c) point (*C*) marked in Fig. 3(b). *U* is the time averaged velocity at the corresponding point. Examples of bursts (rare events) are marked in black. (d) Cross-correlation of normalized velocity fluctuations at points (A), (B), and (C). The colored rectangle indicates the confident band. (e) Power spectral density of velocity fluctuations at points (A), (B), and (C).

indication of the intermittency of the purely elastic turbulent flow, is clearly visible in the velocity fluctuations at all positions [marked in black in Figs. 7(a)–7(c)]. The temporal fluctuations at points (B) and (C) look very similar but differ significantly from point (A). This is further evident in the cross-correlation between time series shown in Fig. 7(d). The significant correlation between points (B) and (C) with a peak at zero lag time implies that fluctuations at these points are highly correlated and synchronized. This indicates the presence of a flow structure, which will be explained in detail in the context of the POD analysis in Sec. IV C.

3. Spectral features

The power spectral densities (PSD) of velocity fluctuations at points (A), (B), and (C) are plotted in Fig. 7(e). A power decay, $\sim f^{-\beta}$, with an exponent of $\beta \approx 2$ describes the power spectral density of the velocity fluctuations in the range of 1 to 10 Hz. Similar exponents have also been reported for the PSD of velocity fluctuations ($\beta \approx 2.3$),[42] stress fluctuations ($\beta \approx 2.0$),[76] and pressure fluctuations ($\beta \approx 2.2$)[38] of semi-dilute entangled polymer solutions in curved geometries. However, at lower frequencies, the exponent is smaller than $\beta \approx 2$. The presence of two different exponents in the PSD curve of velocity fluctuations has been also reported by various researchers, but no clear reasoning for this observation has been provided so far.[38,47] We believe that in our case, the reason for the lower exponent at lower frequencies is the presence of a large turbulent structure that is associated with the secondary flow. This is further supported by the fact that at point (B) and (C), the power corresponding to the low frequencies is larger than in point (A).

It should be noted that the observed exponent of $\beta \approx 2$ for semi-dilute polymer solutions is smaller than the corresponding exponents of $\beta > 3$ commonly reported for purely elastic turbulent flow of dilute polymer solutions.[24,42] The value of $\beta \approx 3$ is theoretically predicted for dilute polymer solutions based on the assumption of homogeneous flow, linear elasticity, and linear relaxation of the polymers, which do not apply to the semi-dilute entangled regime.[24,25,47,77] In fact, as discussed in Sec. III A, the rheological properties of polymer solutions in the semi-dilute entangled regime are shear dependent and, thus, highly nonlinear. Therefore, it is not unexpected that the exponent of the power spectral density of the velocity fluctuations appears to be different from the value for dilute polymer solutions. However, there is so far no theoretical work on the spectral features of purely elastic turbulent flow of semi-dilute entangled polymer solutions and the expected exponents for this concentration regime.

As proposed by de Gennes[78] in "Reptation Theory" and as experimentally demonstrated by Perkins *et al.*,[20] the motion of the entangled polymers is strongly restricted by the neighboring polymers as if they were confined in a tube. Therefore, due to the restricted deformation and freedom of individual polymers, their corresponding back reaction to the flow is also restricted. Furthermore, as shown in Fig. 5,

the rotational component of the flow in the serpentine channel intensifies at high Weissenberg numbers while the extensional component is weakened. This can reduce the extent of polymer stretching and, thus, dampen the corresponding velocity fluctuations.[16]

The damping and limiting of the flow fluctuations are reflected in the smaller exponent of the power decay of the velocity fluctuations, indicating that the range of excited scales in the flow is also limited.

C. Proper orthogonal decomposition of the purely elastic turbulent flow

The cross correlation of velocity fluctuations at points (B) and (C) in conjunction with the PSD analysis points toward an underlying flow structure. In fact, an interesting feature of viscoelastic flow in bend channels is the presence of a secondary flow due to hoop stress caused by the gradient of the first normal stress difference.[13,79,80] However, experimental studies have so far only been able to implicitly indicate the presence of secondary flows based on the bent streamlines in the mean flow direction.[79] As we discussed extensively so far, the turbulent flow of a semi-dilute entangled polymer solution in a serpentine channel is non-homogeneous and anisotropic on any scale. This rejects the assumption of Taylor's hypothesis, and one cannot explain spatial flow properties based on temporal statistics. Therefore, in this section, we will directly extract the secondary turbulent structure using the POD method. As discussed in Sec. II, the aim of proper orthogonal decomposition is to find a hierarchy of spatial modes, $\Phi^{(n)}$, that best describes the original stochastic flow. The energy spectrum of spatial eigenmodes, E_i, calculated at three different Weissenberg numbers above the onset of purely elastic instability is plotted in Fig. 8(a). The first mode in all cases contains the highest energy content, which at the highest stage of the turbulent flow at $Wi \approx 45$ contains almost 50% of the total kinetic energy (TKE) of the system. The first mode, in fact, represents the time averaged mean flow, and all the other modes describe the deviations from the mean flow. The energy content of the modes decays and is less than 1% of TKE for modes larger than 6. As can be seen from the cumulative energy plot in Fig. 8(b), the energy content of the lower modes is higher at higher Weissenberg numbers, i.e., where the elastic stresses are more significant. In fact, at $Wi \approx 45$, the first 375 eigenmodes represent 90% of the TKE, while for $Wi \approx 17$, the number of eigenmodes representing 90% of the TKE is 700. This indicates that at higher Weissenberg numbers, the lower modes representing the larger scale structures gain more energy at the expense of the higher modes, which correspond to the finer structures. It can be concluded that, at higher Weissenberg numbers, only a few early modes are sufficient to describe the existing dominant flow structures in the system. Moreover, an exponent of approximately (−11/9) can be fitted to the energy decay spectrum in the range of 2–40, indicated by a dashed line in Fig. 8(a). The exponent of (−11/9) has been proposed by Knight and Sirovich based on dimensional arguments for the Kolmogorov inertial range in non-homogeneous turbulent flows.[81] Since, in our case, the exponent of $\beta \approx 2$ for the PSD curve of velocity fluctuations is close to the Kolmogorov scale of (5/3), the exponent of about (−11/9) is not unexpected.

In order to gain insight into the dominant flow structures, the vector fields of spatial eigenmodes and their corresponding temporal coefficients of the three initial highest energy modes at $Wi \approx 45$ are illustrated in Fig. 9. It should be noted that although the 2D distribution of these modes resembles the shape of a velocity field, they do not convey the same physical meaning because eigenmodes are, in fact, dimensionless. Indeed, the instantaneous velocity field associated with each mode is computed as $\mathbf{U}^{(n)}(x,y,t) = \mathbf{a}^{(n)}(t) \cdot \mathbf{\Phi}^{n}(x,y)$. The spatial eigenmodes of the first mode, i.e., the mean flow, clearly indicate a strong spiral motion at the lateral sides of the half-bend [Fig. 9(a)]. This points toward the secondary flow governed by the serpentine geometry due to the change in the curvature at the inflection points, (B) and (C), affecting the streamwise mean flow.[79,82] The temporal coefficients associated with the first mode exhibit a sudden jump after a certain time, i.e., the number of snapshots. This sudden jump has also been observed in numerical simulations for viscoelastic Oldroyd-B fluids and is related to the onset of the temporal evolution of the flow.[55]

The presence of counter-rotating vortices associated with hoop stress, caused by the gradient of the first normal stress difference[13,79,80] in the serpentine channel is further evident in the spatial eigenmodes 2 and 3, which contain 5% and 3% of the TKE, respectively, as can be seen in Figs. 9(b) and 9(c).

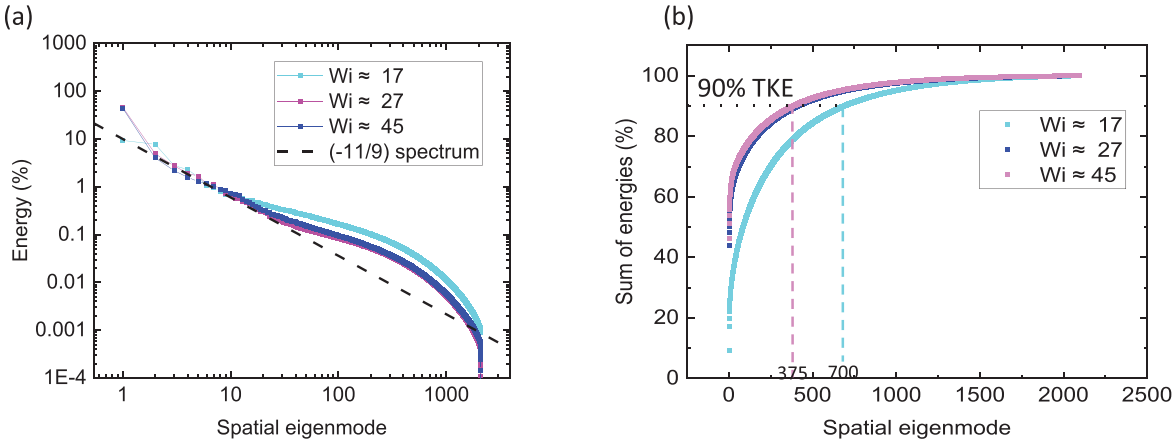

FIG. 8. (a) The energy spectrum of the spatial eigenmodes, the dashed line indicates a spectrum exponent of (−11/9), and (b) the cumulative energy of the spatial eigenmodes. The total number of eigenmodes corresponding to 90% TKE is shown as dashed lines.

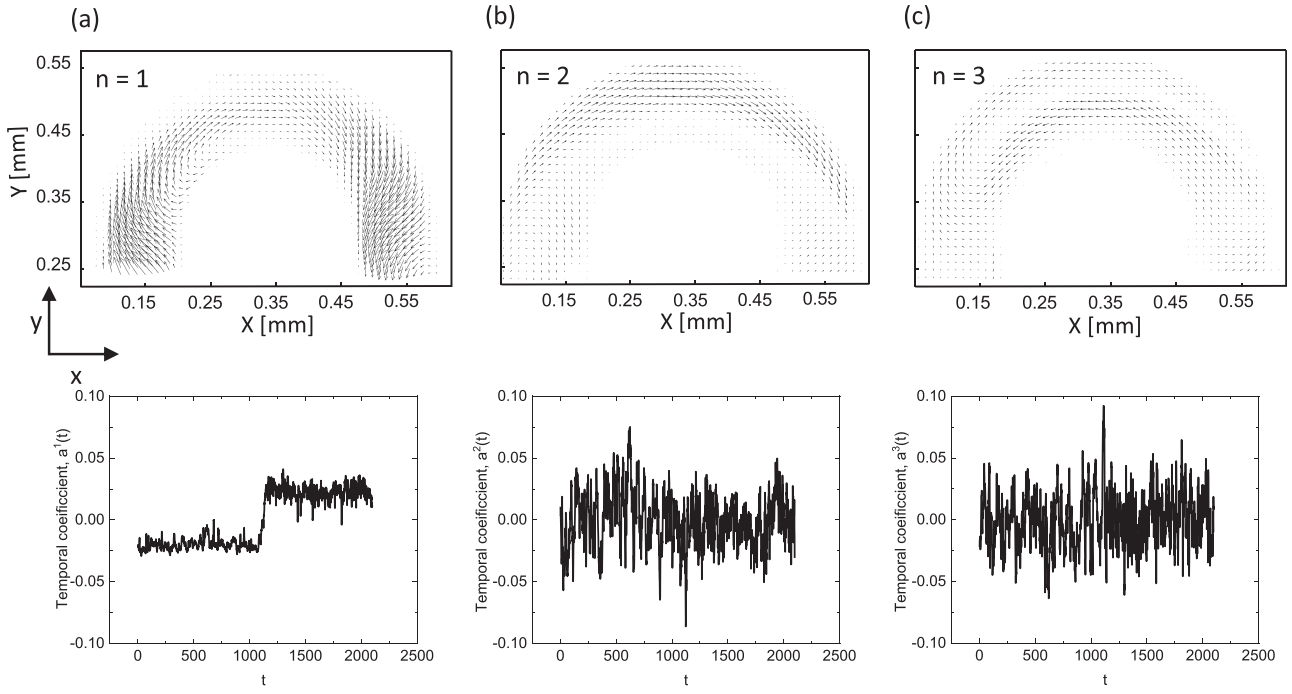

FIG. 9. The vector fields of spatial eigenmodes (top) and their corresponding temporal coefficients (bottom) at $Wi \approx 45$, t is the number of the snapshot or the vector number, for (a) mode 1, (b) mode 2, and (c) mode 3.

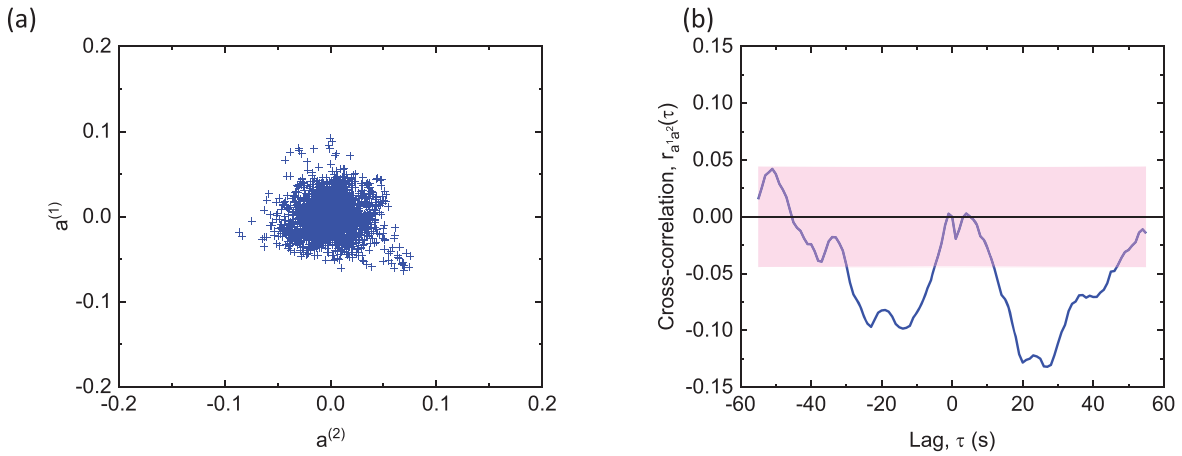

FIG. 10. (a) Phase portrait of temporal coefficients of mode 2 vs mode 3 and (b) cross correlation between temporal coefficients of mode 2 and mode 3. The colored rectangle indicates the confident band.

To clarify the correlation between modes 2 and 3, the time coefficients of these modes are plotted against each other in Fig. 10(a). As evident in the rather compact circular scattering of the temporal coefficients in the phase portrait, the temporal coefficients are strongly related, even though both seem to fluctuate rather randomly. The cross correlation of these temporal coefficients in Fig. 10(b) verifies that modes 2 and 3 are indeed anti-correlated. These observations confirm that at high Weissenberg numbers, there is a strong secondary flow in the form of counter-rotating vortices, which significantly contributes to the total kinetic energy of the system. Therefore, we can conclude that the strong increase in the flow resistance during the flow of the polymer solution in the serpentine channel is indeed related to the activity of the secondary flow caused by the geometry and the significant first normal stress difference at high Weissenberg numbers.

V. CONCLUSION

In this work, we have performed μPIV experiments to extract spatially and temporally high-resolution velocity fields of a semi-dilute

entangled polymer solution flowing in a serpentine channel. The general flow inspections and standard single-point statistical analysis reveal the presence of a highly anisotropic non-homogeneous unstable flow above a critical Weissenberg number. The power spectral density plot decays with an exponent relatively smaller than the corresponding value of a dilute polymer solution. This indicates a limited range of excited scales in the purely elastic turbulent flow of a semi-dilute entangled polymer solution compared to the dilute regime, which is due to the limitation of polymer motion in space and entanglement above the overlap concentration. In addition, the geometry-induced mixed flow type and the strong rotation and weak extension of the flow in the turbulent state further reduce the extent of polymer stretching and, thus, reduce the range of excited scales in the turbulent flow.

The two-point correlation indicates the strong cross correlation between the fluctuations at the two lateral ends of a half-bend. This implies the presence of a strong secondary flow structure. Due to the absence of a global correlation between the velocity fluctuations, and non-homogeneity of the flow and thus invalidity of the Taylor hypothesis, we used the proper orthogonal decomposition method to gain direct insight into the structural properties of the observed purely elastic turbulent flow. The POD analysis, in fact, clearly shows a strong spiral structure in the highest energy mode and counter-rotating vortices in the two subsequent modes. This confirms the existence of a three-dimensional secondary flow driven by the geometry and the hoop stress, which originates from the gradient of the first normal stress difference in the transversal direction between the inner and outer walls.

With this first experimental characterization of the flow of a semi-dilute polymer solution, we hope to stimulate a theoretical validation of the experimentally observed features that will provide a deep insight into the flow and purely elastic turbulence in this concentration regime.

ACKNOWLEDGMENTS

We acknowledge the generous support of ExploRe program of BP plc. We would like to thank SNF Floerger, France, for kindly providing us the Flopaam polymers.

AUTHOR DECLARATIONS

Conflict of Interest

The authors have no conflicts to disclose.

Author Contributions

Pegah Shakeri: Conceptualization (equal); Data curation (equal); Formal analysis (equal); Methodology (equal); Software (equal); Validation (equal); Visualization (equal); Writing – original draft (equal); Writing – review and editing (equal). **Michael Jung:** Conceptualization (equal); Investigation (equal); Methodology (equal); Supervision (equal); Validation (equal); Writing – original draft (equal); Writing – review and editing (equal). **Ralf Seemann:** Conceptualization (equal); Funding acquisition (lead); Project administration (lead); Resources (lead); Supervision (lead); Writing – original draft (equal); Writing – review and editing (equal).

DATA AVAILABILITY

The data that support the findings of this study are available from the corresponding author upon reasonable request.

REFERENCES

[1]M. Rubinstein, R. H. Colby *et al.*, *Polymer Physics* (Oxford University Press, New York, 2003), Vol. 23.
[2]K. S. Sorbie, *Polymer-Improved Oil Recovery* (Springer Science & Business Media, 2013).
[3]J. M. Dealy and K. F. Wissbrun, *Melt Rheology and Its Role in Plastics Processing: Theory and Applications* (Springer Science & Business Media, 2012).
[4]B. Meulenbroek, C. Storm, V. Bertola, C. Wagner, D. Bonn, and W. van Saarloos, "Intrinsic route to melt fracture in polymer extrusion: A weakly nonlinear subcritical instability of viscoelastic Poiseuille flow," Phys. Rev. Lett. **90**, 024502 (2003).
[5]S. E. Spagnolie, *Biological and Medical Physics, Biomedical Engineering* (Springer, 2015).
[6]M. Thiébaud, Z. Shen, J. Harting, and C. Misbah, "Prediction of anomalous blood viscosity in confined shear flow," Phys. Rev. Lett. **112**, 238304 (2014).
[7]M. Levant and V. Steinberg, "Complex dynamics of compound vesicles in linear flow," Phys. Rev. Lett. **112**, 138106 (2014).
[8]S. Gulati, D. Liepmann, and S. J. Muller, "Elastic secondary flows of semidilute DNA solutions in abrupt 90° microbends," Phys. Rev. E **78**, 036314 (2008).
[9]R. B. Bird, C. F. Curtiss, R. C. Armstrong, and O. Hassager, *Dynamics of Polymeric Liquids* (Wiley-Interscience, 1987), Vol. 2.
[10]H. Giesekus, "Zur stabilität von strömungen viskoelastischer flüssigkeiten," Rheol. Acta **5**, 239 (1966).
[11]W. M. Abed, R. D. Whalley, D. J. Dennis, and R. J. Poole, "Experimental investigation of the impact of elastic turbulence on heat transfer in a serpentine channel," J. Non-Newtonian Fluid Mech. **231**, 68–78 (2016).
[12]A. Groisman and V. Steinberg, "Efficient mixing at low Reynolds numbers using polymer additives," Nature **410**, 905 (2001).
[13]P. Shakeri, M. Jung, and R. Seemann, "Effect of elastic instability on mobilization of capillary entrapments," Phys. Fluids **33**, 113102 (2021).
[14]R. H. Ewoldt, M. T. Johnston, and L. M. Caretta, *In Complex Fluids in Biological Systems* (Springer, 2015), pp. 207–241.
[15]K. Hyun, M. Wilhelm, C. O. Klein, K. S. Cho, J. G. Nam, K. H. Ahn, S. J. Lee, R. H. Ewoldt, and G. H. McKinley, "A review of nonlinear oscillatory shear tests: Analysis and application of large amplitude oscillatory shear (LAOS)," Prog. Polym. Sci. **36**, 1697–1753 (2011).
[16]E. Balkovsky, A. Fouxon, and V. Lebedev, "Turbulence of polymer solutions," Phys. Rev. E **64**, 056301 (2001).
[17]Y. Jun and V. Steinberg, "Polymer concentration and properties of elastic turbulence in a von Karman swirling flow," Phys. Rev. Fluids **2**, 103301 (2017).
[18]V. Steinberg, "Scaling relations in elastic turbulence," Phys. Rev. Lett. **123**, 234501 (2019).
[19]C. A. Browne and S. S. Datta, "Elastic turbulence generates anomalous flow resistance in porous media," Sci. Adv. **7**, eabj2619 (2021).
[20]T. T. Perkins, D. E. Smith, and S. Chu, "Direct observation of tube-like motion of a single polymer chain," Science **264**, 819 (1994).
[21]N. Tyagi and B. J. Cherayil, "The relaxation dynamics of single flow-stretched polymers in semidilute to concentrated solutions," J. Chem. Phys. **154**, 024907 (2021).
[22]E. S. Shaqfeh, "The dynamics of single-molecule DNA in flow," J. Non-Newtonian Fluid Mech. **130**, 1 (2005).
[23]P. LeDuc, C. Haber, G. Bao, and D. Wirtz, "Dynamics of individual flexible polymers in a shear flow," Nature **399**, 564 (1999).
[24]A. Fouxon and V. Lebedev, "Spectra of turbulence in dilute polymer solutions," Phys. Fluids **15**, 2060 (2003).
[25]S. Berti, A. Bistagnino, G. Boffetta, A. Celani, and S. Musacchio, "Two-dimensional elastic turbulence," Phys. Rev. E **77**, 055306 (2008).
[26]F. Cruz, R. Poole, A. Afonso, F. Pinho, P. Oliveira, and M. Alves, "Influence of channel aspect ratio on the onset of purely-elastic flow instabilities in three-dimensional planar cross-slots," J. Non-Newtonian Fluid Mech. **227**, 65 (2016).
[27]H. Garg, E. Calzavarini, and S. Berti, "Statistical properties of two-dimensional elastic turbulence," Phys. Rev. E **104**, 035103 (2021).
[28]E. S. Shaqfeh, "Purely elastic instabilities in viscometric flows," Annu. Rev. Fluid Mech. **28**, 129 (1996).

[29]T. Burghelea, E. Segre, and V. Steinberg, "Elastic turbulence in von Karman swirling flow between two disks," Phys. Fluids **19**, 053104 (2007).
[30]S. J. Haward, G. H. McKinley, and A. Q. Shen, "Elastic instabilities in planar elongational flow of monodisperse polymer solutions," Sci. Rep. **6**, 33029 (2016).
[31]X. Shi and G. F. Christopher, "Growth of viscoelastic instabilities around linear cylinder arrays," Phys. Fluids **28**, 124102 (2016).
[32]A. Soulies, J. Aubril, C. Castelain, and T. Burghelea, "Characterisation of elastic turbulence in a serpentine micro-channel," Phys. Fluids **29**, 083102 (2017).
[33]G. Yao, J. Zhao, H. Yang, M. A. Haruna, and D. Wen, "Reynolds number effect on drag control via spanwise wall oscillation in turbulent channel flows," Phys. Fluids **31**, 085108 (2019).
[34]S. S. Datta, A. M. Ardekani, P. E. Arratia, A. N. Beris, I. Bischofberger, J. G. Eggers, J. E. López-Aguilar, S. M. Fielding, A. Frishman, M. D. Graham, J. S. Guasto, S. J. Haward, S. Hormozi, G. H. McKinley, R. J. Poole, A. Morozov, V. Shankar, E. S. G. Shaqfeh, A. Q. Shen, H. Stark, V. Steinberg, G. Subramanian, and H. A. Stone, "Perspectives on viscoelastic flow instabilities and elastic turbulence," arXiv:2108.09841 [physics.flu-dyn] (2021).
[35]R. van Buel and H. Stark, "Characterizing elastic turbulence in the three-dimensional von Kármán swirling flow using the Oldroyd-B model," Phys. Fluids **34**, 043112 (2022).
[36]L. Casanellas, M. A. Alves, R. J. Poole, S. Lerouge, and A. Lindner, "The stabilizing effect of shear thinning on the onset of purely elastic instabilities in serpentine microflows," Soft Matter **12**, 6167–6175 (2016).
[37]A. M. Howe, A. Clarke, and D. Giernalczyk, " Flow of concentrated viscoelastic polymer solutions in porous media: Effect of M W and concentration on elastic turbulence onset in various geometries," Soft Matter **11**, 6419–6431 (2015).
[38]D. Kawale, E. Marques, P. L. Zitha, M. T. Kreutzer, W. R. Rossen, and P. E. Boukany, "Elastic instabilities during the flow of hydrolyzed polyacrylamide solution in porous media: Effect of pore-shape and salt," Soft Matter **13**, 765 (2017).
[39]X. Chen, H. Marschall, M. Schäfer, and D. Bothe, "A comparison of stabilisation approaches for finite-volume simulation of viscoelastic fluid flow," Int. J. Comput. Fluid Dyn. **27**, 229 (2013).
[40]H.-C. Tseng, "A revisitation of White−Metzner viscoelastic fluids," Phys. Fluids **33**, 057115 (2021).
[41]K. Tatsumi, Y. Takeda, K. Suga, and K. Nakabe, "Turbulence characteristics and mixing performances of viscoelastic fluid flow in a serpentine micro-channel," J. Phys.: Conf. Ser. **318**(9), 092020 (2011).
[42]Y. Jun and V. Steinberg, "Power and pressure fluctuations in elastic turbulence over a wide range of polymer concentrations," Phys. Rev. Lett. **102**, 124503 (2009).
[43]A. Malm and T. Waigh, "Elastic turbulence in entangled semi-dilute DNA solutions measured with optical coherence tomography velocimetry," Sci. Rep. **7**, 1186 (2017).
[44]R. Lindken, M. Rossi, S. Große, and J. Westerweel, "Micro-particle image velocimetry (μPIV): Recent developments, applications, and guidelines," Lab Chip **9**, 2551 (2009).
[45]S. J. Beresh, "Time-resolved particle image velocimetry," Meas. Sci. Technol. **32**, 102003 (2021).
[46]A. Schröder and C. E. Willert, *Particle Image Velocimetry: New Developments and Recent Applications* (Springer Science & Business Media, 2008), Vol. 112.
[47]A. Groisman and V. Steinberg, "Elastic turbulence in curvilinear flows of polymer solutions," New J. Phys. **6**, 29 (2004).
[48]B. Qin and P. E. Arratia, "Characterizing elastic turbulence in channel flows at low Reynolds number," Phys. Rev. Fluids **2**, 083302 (2017).
[49]S. J. Muller, R. G. Larson, and E. S. Shaqfeh, "A purely elastic transition in Taylor-Couette flow," Rheol. Acta **28**, 499 (1989).
[50]T. Burghelea, E. Segre, and V. Steinberg, "Validity of the Taylor hypothesis in a random spatially smooth flow," Phys. Fluids **17**, 103101 (2005).
[51]G. I. Taylor, "The spectrum of turbulence," Proc. Roy. Soc. London, Ser. A **164**, 476 (1938).
[52]G. Berkooz, P. Holmes, and J. L. Lumley, "The proper orthogonal decomposition in the analysis of turbulent flows," Annu. Rev. Fluid Mech. **25**, 539 (1993).
[53]E. De Angelis, C. M. Casciola, V. S. L'vov, R. Piva, and I. Procaccia, "Drag reduction by polymers in turbulent channel flows: Energy redistribution between invariant empirical modes," Phys. Rev. E **67**, 056312 (2003).
[54]K. D. Housiadas, A. N. Beris, and R. A. Handler, "Viscoelastic effects on higher order statistics and on coherent structures in turbulent channel flow," Phys. Fluids **17**, 035106 (2005).
[55]P. Gutierrez-Castillo and B. Thomases, "Proper orthogonal decomposition (POD) of the flow dynamics for a viscoelastic fluid in a four-roll mill geometry at the Stokes limit," J. Non-Newtonian Fluid Mech. **264**, 48 (2019).
[56]P. Holmes, J. L. Lumley, G. Berkooz, and C. W. Rowley, *Turbulence, Coherent Structures, Dynamical Systems and Symmetry* (Cambridge University Press, 2012).
[57]J. L. Lumley, *Transition and Turbulence* (Elsevier, 1981), pp. 215–242.
[58]B. Podvin and Y. Fraigneau, "A few thoughts on proper orthogonal decomposition in turbulence," Phys. Fluids **29**, 020709 (2017).
[59]K. Taira, S. L. Brunton, S. T. Dawson, C. W. Rowley, T. Colonius, B. J. McKeon, O. T. Schmidt, S. Gordeyev, V. Theofilis, and L. S. Ukeiley, "Modal analysis of fluid flows: An overview," AIAA J. **55**, 4013 (2017).
[60]P. J. Schmid, D. S. Henningson, and D. Jankowski, "Stability and Transition in Shear Flows. Applied Mathematical Sciences, Vol. 142," Appl. Mech. Rev **55**, B57 (2002).
[61]L. Sirovich, "Turbulence and the dynamics of coherent structures. I. Coherent structures," Q. Appl. Math. **45**, 561 (1987).
[62]A. Chatterjee, Curr. Sci. **78**, 808 (2000), available at https://www.jstor.org/stable/24103957.
[63]API, *API Recommended Practice 63 (RP63)* (API, 1990).
[64]A. Clarke, A. M. Howe, J. Mitchell, J. Staniland, and L. A. Hawkes, "How viscoelastic-polymer flooding enhances displacement efficiency," SPE J. **21**, 0675 (2016).
[65]P. Shakeri, M. Jung, and R. Seemann, "Scaling purely elastic instability of strongly shear thinning polymer solutions," Phys. Rev. E **105**, L052501 (2022).
[66]H. A. Barnes, J. F. Hutton, and K. Walters, *An Introduction to Rheology* (Elsevier, 1989), Vol. 3.
[67]O. Maklad and R. Poole, "A review of the second normal-stress difference; its importance in various flows, measurement techniques, results for various complex fluids and theoretical predictions," J. Non-Newtonian Fluid Mech. **292**, 104522 (2021).
[68]J. L. White and A. B. Metzner, "Development of constitutive equations for polymeric melts and solutions," J. Appl. Polym. Sci. **7**, 1867–1889 (1963).
[69]T. Burghelea and V. Bertola, *Transport Phenomena in Complex Fluids* (Springer, 2020), Vol. 598.
[70]Y. Xia and G. M. Whitesides, "Soft lithography," Annu. Rev. Mater. Sci. **28**, 153–184 (1998).
[71]M. Olsen and R. Adrian, "Out-of-focus effects on particle image visibility and correlation in microscopic particle image velocimetry," Exp. Fluids **29**, S166 (2000).
[72]J. Westerweel, "Fundamentals of digital particle image velocimetry," Meas. Sci. Technol. **8**, 1379 (1997).
[73]Y. Son, "Determination of shear viscosity and shear rate from pressure drop and flow rate relationship in a rectangular channel," Polymer **48**, 632–637 (2007).
[74]P. D. Gennes, "Coil-stretch transition of dilute flexible polymers under ultra-high velocity gradients," J. Chem. Phys. **60**, 5030 (1974).
[75]S. J. Haward, C. C. Hopkins, and A. Q. Shen, "Stagnation points control chaotic fluctuations in viscoelastic porous media flow," Proc. Natl. Acad. Sci. **118**, e2111651118 (2021).
[76]J. Beaumont, N. Louvet, T. Divoux, M.-A. Fardin, H. Bodiguel, S. Lerouge, S. Manneville, and A. Colin, "Turbulent flows in highly elastic wormlike micelles," Soft Matter **9**, 735 (2013).
[77]M. Grilli, A. Vázquez-Quesada, and M. Ellero, "Transition to turbulence and mixing in a viscoelastic fluid flowing inside a channel with a periodic array of cylindrical obstacles," Phys. Rev. Lett. **110**, 174501 (2013).
[78]P.-G. D. Gennes, "Reptation of a polymer chain in the presence of fixed obstacles," J. Chem. Phys. **55**, 572 (1971).

[79]L. Ducloué, L. Casanellas, S. J. Haward, R. J. Poole, M. A. Alves, S. Lerouge, A. Q. Shen, and A. Lindner, "Secondary flows of viscoelastic fluids in serpentine microchannels," Microfluid. Nanofluid. **23**, 33 (2019).
[80]R. Poole, A. Lindner, and M. Alves, "Viscoelastic secondary flows in serpentine channels," J. Non-Newtonian Fluid Mech. **201**, 10 (2013).
[81]B. Knight and L. Sirovich, "Kolmogorov inertial range for inhomogeneous turbulent flows," Phys. Rev. Lett. **65**, 1356 (1990).
[82]L. Guglielmini, R. Rusconi, S. Lecuyer, and H. A. Stone, "Three-dimensional features in low-Reynolds-number confined corner flows," J. Fluid Mech. **668**, 33–57 (2011).